Research Square

Preprints are preliminary reports that have not undergone peer review.
They should not be considered conclusive, used to inform clinical practice,
or referenced by the media as validated information.

Reconstructing the Velocity Field of Internal Waves from Continental Shelf Stratification

Rizwan Qayyum
National University of Sciences and Technology
Alex Sheremet
alex@coastal.ufl.edu

University of Florida

Research Article

Keywords: internal waves, flow reconstruction, stratification, continental shelf, Inner Shelf Dynamics Experiment, geo-strophic inversion

Posted Date: November 17th, 2026

DOI: https://doi.org/10.21203/rs.3.rs-11568246/v1

License: This work is licensed under a Creative Commons Attribution 4.0 International License.
Read Full License

Additional Declarations: No competing interests reported.

Reconstructing the Velocity Field of Internal Waves from Continental Shelf Stratification

Rizwan Qayyum[1] and Alex Sheremet[2*]

[1]Military College of Engineering, National University of Sciences & Technology, Islamabad, Pakistan.

[2]Engineering School of Sustainable Infrastructure and Environment, University of Florida, Gainesville FL 32611, USA.

*Corresponding author(s). E-mail(s): alex@coastal.ufl.edu;
Contributing authors: qarizwan@mce.nust.edu.pk;

Abstract

Obtaining direct flow measurements on the ocean shelf (∼100-m depth) is expensive in general, and highly challenging in inaccessible shelf areas. In contrast, stratification information is relatively easier to obtain, for example, using acoustic sounding techniques. Retrieving the flow information from stratification data is a classical geostrophic flow problem in meteorology, but its usefulness in understanding the dynamics of other stratified flows remains unclear. Here, we investigate the velocity reconstruction from stratification for internal waves, using the simplest approach: the linearized governing equations applied to several simplified, layered stratification representations. The method is tested and validated using field observations collected during the Inner Shelf Dynamics Experiment 2017. Our results show that for internal waves (periods between 5 and 60 min) the approach produces velocity estimates within 0.1 (normalized) deviation from observations. Wave nonlinearity does not appear to cause significant errors: internal wave group *B*, demonstrably more nonlinear by an Ursell-number diagnostic than group *A*, is reconstructed with comparable accuracy, which we attribute to the reconstruction inheriting the nonlinear phase coupling directly from the observed reference variable rather than requiring it to be modeled explicitly. The interaction with large scale flows is partially represented as a slowly varying background; a ≈5-m offset of the reconstructed zero-velocity layer at the 50-m station, present for one of the two events examined and absent for the other, cannot be accounted for by local wind-driven Ekman forcing at the depth where it occurs; barotropic tide and non-local wind-driven circulation, neither of which can be resolved from stratification alone, remain the most likely sources of this residual disagreement. With further refinements, this approach could enhance the usefulness of stratification data for understanding processes such as baroclinic conversion, nonlinear

internal wave evolution, near-bed sediment transport by internal waves (Jefferson et al., 2025), the formation of deep water bedforms, and others.

Keywords: internal waves, flow reconstruction, stratification, continental shelf, Inner Shelf Dynamics Experiment, geo-strophic inversion

1 Introduction

Direct field observations of internal wave flows on a stratified shelf are scarce, and generally do not resolve well aspects of wave dynamics such as baroclinic to barotropic conversion, bottom and surface boundary layers, and spatio-temporal transformation of stratification perturbations (Klymak and Moum, 2003; Hosegood et al., 2004; Quaresma et al., 2007; La Forgia et al., 2019; Reeder et al., 2011; Zulberti et al., 2020). One of the reasons is the wide range of scales involved, from 100 km (barotropic tide) to 100 m (internal waves), with vertical scales from 100 m to 1 m in the bottom boundary layer. No existing measurement system is capable of resolving well this scale span. Moreover, deploying existing measuring systems, limited as they are (e.g., in situ moorings and bottom mounted instruments) at shelf depths in the order of 100 m is expensive and difficult.

A popular method for observing internal waves in the field is to measure ocean stratification using acoustic means, such as echosounders (Proni and Apel, 1975; Haury et al., 1983; Duda and Farmer, 1999; Farmer and Smith, 1980; Kaye, 2005; Li et al., 2009), seismic profiling (Holbrook et al., 2003; Krahmann et al., 2008; Ruddick et al., 2009; Sheen et al., 2009; Gunn et al., 2021), or tethered profilers (Krishfield et al., 2008; Toole et al., 2010). Such remote sensing measurements are arguably easier to obtain, do not require in situ deployments of bottom mounted instrumentation, and provide a detailed map of density stratification with a wide scale coverage (e.g., Holbrook et al., 2003). The ability of echosounding data to resolve internal waves has been examined before through comparisons with in situ measurements (e.g., Li et al., 2009). Retrieving the flow from remote observations may be formulated as data assimilation, or as an inverse modeling approach (e.g., Pica et al., 1990) that complement stratification information with other data sources (e.g., free surface elevation), and use of advanced multiscale circulation models and field observations. However, the numerical modeling involved for resolving these processes is also highly complex and involves a dedicated, significant effort. In the meantime, the usefulness of stratification information as a standalone data source for estimating the flow remains unclear, and, as a consequence, inferring dynamics solely from stratification information remains tenuous.

Here, we consider the problem of retrieving flow information from the observations of stratification on the continental shelf. To be useful as a standalone data source, stratification information (density, temperature) must meet two obvious basic conditions of existence and sensitivity: the water column density or temperature gradient must be measurable and nonzero, and must exhibit measurable perturbations. These conditions exclude, for example, well mixed environments, or, alternatively, well stratified flows dominated by barotropic processes such as large scale, wind driven circulation and barotropic tides. This is not a peripheral caveat but a defining boundary of the approach: because barotropic wind-driven (Ekman) currents and barotropic tides do not, to leading order, perturb the density field, they are by

construction invisible to a reconstruction that uses only stratification as input, regardless of how well the baroclinic component is resolved. This limitation is revisited quantitatively in section 4, where it is shown to be a contributing factor behind the residual disagreement between reconstructed and observed velocity at one of the two field sites. A natural path toward removing this limitation, left here for future work (see section 4), is to supply the missing barotropic information externally, e.g., from a regional barotropic tide inversion such as OTIS/OTPS (Egbert et al., 1994; Egbert and Erofeeva, 2002), rather than attempting to infer it from stratification. As a consequence, the scope of reconstructing the flow from stratification is limited to baroclinic processes.

Specific to the continental shelf, there are additional challenges. The spatial extent of large scale processes may involve a wide range of depths, boundary effects due to the proximity of coasts, including subdomains with different mixing characteristics (e.g., breaking regions), as well as refraction, reflection, standing wave patterns etc. All these processes are typically not resolvable by analyzing local stratification data. The shelf environment is also characterized by significant nonlinear evolution and scale coupling. The coupled dynamics of barotropic tides and internal waves may be described as a scale cascade, with barotropic tides transferring energy to baroclinic tides (baroclinic conversion problem; Bell, 1975; Baines, 1982; Smith and Young, 2002; Nycander, 2005; Shakespeare, 2020; Shakespeare et al., 2020); which in turn evolve nonlinearly and disintegrate into trains of internal waves (Pelinovsky et al., 1994; Holloway et al., 1999; Holloway, 2001; Helfrich and Melville, 2006; Grimshaw et al., 2010). This implies, on the one hand, that large scale barotropic and baroclinic processes cannot be globally separated, and on the other, that local scale processes (internal waves) evolve significantly on large scales.

Despite all these challenges, the idea of retrieving the flow information from stratification data is attractive for many reasons: it can help with understanding flow processes/features such as barotropic/baroclinic partition (usually done by inferring vertical scale separation, e.g., Edwards and Seim, 2008); baroclinic conversion; nonlinear generation of internal waves; near-bed sediment transport by internal waves (Quaresma et al., 2007; Zulberti et al., 2020); formation of deep water bedforms (Ma et al., 2016), as well as underwater acoustics applications (Chiu and Reeder, 2013; Chiu et al., 2015). To the best of our knowledge, this problem has not been studied. While one may imagine (as above) its up- and downsides, in reality its effectiveness and limitations are not understood.

The practical relevance of the instrumentation-substitution idea is illustrated directly by a companion analysis of the same Inner Shelf Dynamics Experiment dataset: using the 35-m station velocity profiler record, Jefferson et al. (2025) show that near-bed velocity associated with internal tide/wave phase coupling is consequential for sediment resuspension on this shelf, with resuspension occurring preferentially under internal wave crests. That result was obtained from a site that carried a velocimeter; the approach developed here asks whether the near-bed velocity field required for such an analysis can instead be obtained where no velocimeter is deployed at all, using only the stratification record already available from a temperature chain. Framed this way, the present study is a methodological refinement of an established geostrophic inversion technique, applied here to an ageostrophic problem (internal waves), rather than a claim of new internal-wave dynamics; its value is assessed by whether it can stand in for direct velocimetry in exactly the kind of application that Jefferson et al. (2025) demonstrates matters.

Because there is no prior such knowledge, to test effectiveness and limitations, in this study we confine our discussion to small scale baroclinic perturbations (internal waves). We formulate the approach within the simplest, linearized governing equations, and examine also several simplified, layered stratification representations. Section 2 describes mathematical models of internal wave used for estimating the velocity field due to barotropic perturbations, and provides the details of the reconstruction methodology.

We test our approach using field observations collected during the Inner Shelf Dynamics Experiment 2017 (Feddersen et al., 2016; McSweeney et al., 2019; Waterhouse et al., 2020; Kumar et al., 2021), a large collaborative effort to observe stratified flows on the shelf off point Sal, CA, during August and September 2017. The experiment produced a rich data set covering much of the scales of interest for internal stratified flows, discussed in several papers (Colosi et al., 2018; McSweeney et al., 2019; Kumar et al., 2019; Gough et al., 2023; Jefferson et al., 2025). Because integrating the various data sources is also a significant effort (e.g., Celona et al., 2021), we use here a small part of the observations collected by the Naval Research Laboratory. The data is discussed in section 3, with a focus on the elements necessary for the application and validation of the method.

Two properties of this dataset, both discussed in section 3, shape the scope of the validation that follows and are stated here for clarity. First, full-water-column velocity is available only at the 50-m station; at the 35-m station the velocity profiler resolves only the lowest 1.8 m of the water column, so validation of the reconstructed velocity there is necessarily restricted to a near-bed comparison rather than a full-profile one. Second, the reconstruction as formulated recovers the velocity magnitude along a single horizontal propagation direction and does not by itself resolve that direction. The propagation direction was estimated independently from the observed u, v hodograph and is used only to project the reconstructed velocity onto the measured components for comparison. Neither limitation affects the reconstruction procedure itself, which does not use the propagation angle until this comparison step.

Reconstruction results are presented in section 3. Some aspects of their significance are discussed in Section 4. The appendices provide the details of the solution of the governing equations for the layered stratification models used in this study, and a basic summary of the Gardner equation, used here as a paradigmatic model for internal wave nonlinearity.

2 Reconstruction approach

The goal of this study is to investigate a reconstruction method to estimate the flow velocity associated with internal waves, as detected from some spatial information about the water column stratification. The principle is deceivingly simple: assume that enough stratification features are observed to allow for the use the governing equations to estimate the state variables. Because this problem has not been investigated before, we proceed using a simple linear model.

2.1 The linear model for internal waves

Baroclinic perturbations are assumed adiabatic deviations of a stably stratified fluid at rest

$$\varphi(\mathbf{r},z,t) = \overline{\rho}(z) + \widetilde{\rho}(\mathbf{r},z,t), \tag{1}$$

where φ, $\overline{\rho}$, and $\widetilde{\rho}$ are the instantaneous density, the background density, and the density deviation from background value. The variables are the time t, the horizontal position vector $\mathbf{r} = (x, y)$, and the vertical coordinate z with the origin at the sea bottom. With this separation, the linearized equations are (e.g., Gerkema and Zimmerman, 2008)

$$\frac{\partial \widetilde{\mathbf{u}}}{\partial t} + f\widehat{\mathbf{z}} \times \widetilde{\mathbf{u}} = -\frac{1}{\overline{\rho}} \nabla \widetilde{p}; \quad \widetilde{w}_t = -\frac{1}{\rho_*} \frac{\partial \widetilde{p}}{\partial z} + \widetilde{b}; \tag{2}$$

$$\frac{\partial \widetilde{b}}{\partial t} + wN^2 = 0, \tag{3}$$

$$\nabla \cdot \widetilde{\mathbf{u}} + \frac{\partial \widetilde{w}}{\partial z} = 0; \tag{4}$$

where the unknown functions are the horizontal and vertical components of the velocity $\widetilde{\mathbf{u}} = \widetilde{u}\widehat{\mathbf{x}} + \widetilde{v}\widehat{\mathbf{y}}$ and $\widetilde{w}$, the pressure $\widetilde{p}$, and the buoyancy

$$\widetilde{b} = -g\frac{\widetilde{\rho}}{\rho_*}, \tag{5}$$

where ρ_* is the mean water column density. In equations (2-3) $\nabla = \widehat{\mathbf{x}}\frac{\partial}{\partial x} + \widehat{\mathbf{y}}\frac{\partial}{\partial y}$ is the horizontal gradient operator, $\widehat{\mathbf{x}}$, $\widehat{\mathbf{y}}$, and $\widehat{\mathbf{z}}$ are unit vectors in the direction of the axes, N is the Brunt-Väisälä frequency,

$$N^2 = -\frac{g}{\rho_*}\frac{\partial \overline{\rho}}{\partial z}, \tag{6}$$

and $f = 2\Omega \sin\phi$ is the Coriolis parameter, with ϕ the latitude. The general solution of equations (2-3) may be written as a summation over Fourier modes, for example,

$$\widetilde{q}(\mathbf{r}, z, t) = \sum_{\omega, \mathbf{k}} Q(\mathbf{k}, z, \omega)\, e^{i(\mathbf{k}\cdot\mathbf{r} - \omega t)}, \quad Q_\omega(\mathbf{k}, z, \omega) = \iiint_{-\infty}^{\infty} \widetilde{q}(\mathbf{r}, z, t) e^{-i(\mathbf{k}\cdot\mathbf{r} - \omega t)} dt dx dy \tag{7}$$

where ω is the radian frequency, $\mathbf{k}(\omega) = (k_x, k_y) = k(\widehat{\mathbf{x}}\cos\theta + \widehat{\mathbf{y}}\sin\theta)$ is the horizontal wavenumber vector, and θ is the propagation angle with respect to the x axis. As in equation (7), we use lower/upper case letters to denote a Fourier pair, for example, $(\widetilde{u}, U)$ for the horizontal velocity. Substituting the Fourier representation (7) into equations (2-3) and using the orthogonality of the Fourier modes obtains for the Fourier amplitudes (upper case)

$$\begin{bmatrix} U \\ V \end{bmatrix} = \left(\frac{i}{k}\frac{\mathbf{k}}{k} + \frac{f}{\omega k}\widehat{\mathbf{z}} \times \frac{\mathbf{k}}{k} \right) \frac{dW}{dz}, \tag{8}$$

$$\frac{dP}{dz} = i\rho_* \frac{\omega^2 - f^2}{\omega k^2}\frac{dW}{dz}, \tag{9}$$

$$B = -i\frac{N^2(z)}{\omega} W, \tag{10}$$

and from the continuity equation (4) the Taylor-Goldstein equation

$$\frac{d^2W}{dz^2} + k^2 \frac{N^2(z) - \omega^2}{\omega^2 - f^2} W = 0. \tag{11}$$

Equation (11) is solved here with the boundary conditions

$$W\Big|_{z=0} = W\Big|_{z=h} = 0, \tag{12}$$

where the bottom slope is neglected.

The system (11-12) is a Sturm-Liouville problem with eigenvalue k and eigenfunction $W(z,\omega)$. The problem has a countable set of eigenvalues (e.g., Miropol'sky, 2001): for every given frequency ω, there is a countable set of modes defined by eigenvalue $k_n(\omega)$ and eigenfunction $\psi_n(\omega)$, where $n \in \mathbb{N}$ is the order of the eigenvalue. The set of eigenfunctions is complete and orthogonal in the Hilbert space of square integrable functions with inner product

$$\langle \psi_m, \psi_n \rangle = \int_0^h \frac{N^2(z) - \omega^2}{\omega^2 - f^2} \psi_m \psi_n^* dz = \delta_{mn} \|\psi_m\|^2, \tag{13}$$

$$\|\psi_m\|^2 = \int_0^h \frac{N^2(z) - \omega^2}{\omega^2 - f^2} \psi_m^2 dz, \tag{14}$$

where δ_{mn} is the Kronecker delta. Using eigenfunctions of unit norm $\|\psi_m\|^2 = 1$, a function $W(z,\omega)$ satisfying the boundary conditions admits a unique decomposition of the form

$$W(z,\omega) = \sum_n \alpha_n(\omega) \psi_n(z,\omega), \text{ with } \alpha_n(\omega) = \langle W(z,\omega), \psi_n^*(z,\omega) \rangle. \tag{15}$$

If the vertical modes $\psi_{\omega n}$ are known, the unknown functions in the physical domain (equations 2-4) are obtained using the transfer functions (8-10) and the Fourier representation (7). For example, from equation (8), for a given ω,

$$\begin{bmatrix} U \\ V \end{bmatrix} = \sum_{n,\theta} \frac{\alpha_n}{k_n} \left(i \begin{bmatrix} \cos\theta_n \\ \sin\theta_n \end{bmatrix} + \frac{f}{\omega} \begin{bmatrix} -\sin\theta_n \\ \cos\theta_n \end{bmatrix} \right) \frac{d\psi_n}{dz}. \tag{16}$$

2.2 Flow field reconstruction procedure

The reconstruction procedure described here estimates the quantities associated with the perturbation due to internal waves, denoted by variables marked by tilde, e.g., the velocity $\tilde{\mathbf{u}}$. We assume that $N^2(z)$ and $\widetilde{b}(z,t)$ are known, either from the full density stratification $\rho(z,t)$, or from some information about the background and oscillatory components $\overline{\rho}(z)$ and $\widetilde{\rho}(z,t)$. The flow reconstruction based on the linear model includes the following steps:

1. In the observation data, separate "background" and "perturbation", and estimate $N^2(z)$ and $B_{obs}(z,\omega)$, with B_{obs} the Fourier transform of $\widetilde{b}$; this defines the frequency grid ω, and provides the coefficient of equation (11).

2. Solve the Sturm-Liouville problem (11-12) to obtain the eigenvalues $k_{\omega n}$ and normalized eigenfunctions $\psi_{\omega n}$.
3. Using the observed buoyancy $\widetilde{b}$ as a reference variable, obtain the modal amplitudes $\beta_{\omega n}$ of the observed buoyancy B_{obs} by projecting on the eigenfunctions ψ_{mn} (e.g., equation 15),

$$B_{obs}(z,\omega) = \sum_n \beta_n(\omega)\psi_n(z,\omega), \text{ with } \beta_n(\omega) = \langle B_{obs}(z,\omega), \psi_n^*(z,\omega)\rangle . \tag{17}$$

4. Use equations (8-10) to reconstruct the flow field characteristics. Note that in conditions of interest here, that support internal interfacial waves, $N^2(z)$ is expected to be small outside the interfacial layer. The equation (10) is therefore ill conditioned and cannot be generally inverted pointwise, but may be solved using a pseudoinverse approach. Substituting the expression of the inner product 13 into equation 15, some straightforward algebra obtains the linear system

$$(\mathbf{A}+\mathbf{I})\,\mathbf{a} = \mathbf{b}, \tag{18}$$

where $\mathbf{a} = [\alpha_n]$, $\mathbf{I}$ is the identity matrix, and

$$\mathbf{A} = \frac{\omega^2}{\omega^2 - f^2}\left[\int_0^h \psi_m \psi_n^* dz\right], \; \mathbf{b} = \frac{i\omega}{\omega^2 - f^2}\left[\int_0^h B\psi_n^* dz\right]. \tag{19}$$

Depending on the quality of available observations, one might have to use a simplified, layered stratification model as a substitute for $\overline{\rho}(z,t)$. We examine here two such approximations: the classical model of two homogeneous layers, and a three-layer model with a linearly stratified layer between the two homogeneous layers. In the three-layer model used here, the density is a piecewise linear function

$$\overline{\rho}\,(z) = \begin{cases} \rho_L, & 0 < z < h_L \\ (1-a)\rho_L + a\rho_U, & h_L \le z \le h_L + h_M \\ \rho_U, & h_L + h_M < z \le h \end{cases}, \quad \text{with } a(z) = \frac{z - h_L}{h_M} \tag{20}$$

where $h_{L,M,U}$ are the heights of the lower, middle, and upper layers, respectively, h is the total water depth, and the densities of the lower and upper layer $\rho_L > \rho_U$ are constant. The corresponding Brunt-Väisälä frequency is given by

$$N_M^2 = 2\frac{g\,(\rho_L - \rho_U)}{h_M\,(\rho_L + \rho_U)} > 0 \text{ for } h_L \le z \le h_L + h_M;\; 0 \text{ otherwise.} \tag{21}$$

The two layer-model is a degenerate case of equations corresponding to $h_M = 0$.

Layered stratification models have the advantage that the linear problem has in principle closed analytical solutions. While the two-layer model is widely used in internal wave studies, it only supports one vertical mode. In contrast, three-layer models support a countable set of vertical modes and offer more flexibility in describing flow shear (e.g., Tseluiko et al., 2023), surface bubbly layers (e.g., Grimshaw and Khusnutdinova, 2004), and wave nonlinearity (e.g., Kurkina et al., 2015; Doak et al., 2022; Tseluiko et al., 2023). While most models assume layers of constant density, layers with continuously varying density have been used before

(e.g., exponential – Aksenov et al. 1987; Miropol'sky 2001). The piecewise linear model (20) has been used in studies of internal ship waves by Keller and Munk (1970), and Dysthe and Trulsen (1989). The solution of the linear model with stratification given by (20) (and two layers, with $h_M = 0$) is given in appendix A.

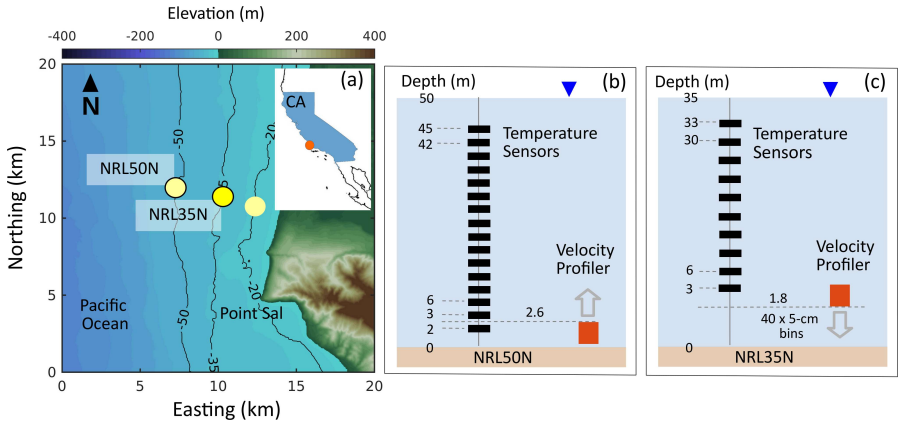


Fig. 1: a) Bathymetry of experiment site with the approximate location of the mooring arrays (yellow circles) deployed by the Naval Research Laboratory. Inset: map of California and Point Sal (red circle). b-c) Schematics of 50-m (NRL50N) and 35-m (NRL35N) moorings (see text for details).

The two layer stratification model requires a different reconstruction approach, because both N^2 and $\widetilde{b}$ are zero in the entire water column. Instead of the observed buoyancy, a set of material surfaces such as the pycnocline (two-layer model), layer interfaces (three-layer model) may be used as a reference quantity. At a fixed location $\mathbf{r} = 0$, the material surfaces $\zeta_n(t)$, $n = 1, 2, \cdots, n_z$,

$$z = z_{0n} + \zeta_n(t), \; n = 1, 2, \cdots, n_z \tag{22}$$

satisfy the linearized equations

$$\frac{\partial \zeta_n}{\partial t} - w = 0, \quad W(z_{0n}, \omega) = -i\omega Z_n(\omega), \qquad \text{on } z = z_{0n}, \tag{23}$$

where (ζ_n, Z_n) are Fourier pairs. Using this representation, step 3 above is replaced with

(3') Determine n_z or less modal amplitudes $\alpha_{\omega n}$ (equation 15) using the system of equations (23).

We will refer to the method using step (3) as the "global" estimator, the one using step (3') as the "local" estimator. For simplicity, we apply here the local estimator for a single material surface, i.e., $n_z = 1$ to estimate only the first vertical mode $\psi_{\omega 0}$.

3 A test using field observations

3.1 Field observations

To test the reconstruction procedure we use here field observations collected by two moorings deployed by the Naval Research Laboratory near the 50-m and 35-m isobaths (figure 1a), during September 2017 on the inner shelf off Point Sal, California, as a part of the Inner Shelf Dynamics Experiment. Figure 1b shows a schematic of the instrument configuration used in this analysis. Both moorings included chains of SBE-56 temperature sensors spaced 3 m apart (15 and 10 units at 50-m and 35-m locations, respectively, sampling continuously at 1 Hz). At the 50-m deep station, the flow velocity was measured using an up-looking Teledyne Marine Sentinel V acoustic Doppler current profiler (ADCP), sampling continuously at 2 Hz, in 47 bins of 0.9-m height (transducer position 2.84 m above the bed). At the 35-m location, the vertical profile of the velocity was recorded using a down-looking Nortek Aquadopp sampling at 2 Hz in 30-min bursts (2400 samples per burst, 20 min burst duration) in 40 vertical bins of 5 cm height covering 2 m water column above bed (transducer position ≈2 m above the bed). Salinity was sampled at 1 Hz using a SeaBird CTD mounted at 2.74 m above the bed.

As noted in section 1, this instrument configuration means that the 35-m velocity record is confined to the lowest 1.8 m of a 35-m water column; effectively the bottom boundary layer, while the 50-m station carries a full-column ADCP. Consequently the 50-m station is used below for the complete-profile validation of the reconstruction (section 3.3), and the 35-m station serves as the near-bed test case that is directly relevant to the sediment mobilization application of Jefferson et al. (2025).

Figures 2–3 show an overview of the stratification observations observed between Sept 15–16th, 2017. At both observation locations, isopycnals (spaced at ≈ 0.22 kg/m^3, figures 2a and 3a) appear to cluster near the mid water column height, in agreement with the vertical structure of N^2 (figures 2b and 3b). The clustering is better defined during time intervals when isopycnals exhibit relatively fast oscillations, for example, events A and B, marked with red rectangles.

The vertical structure of the stratification suggests two classes of oscillation patterns: groups of oscillations with periods in the order of 20 min, superposed on a quasi-stationary slow oscillation on a time scale of 6–12 hours, which may be identified as internal waves and internal tides, respectively. This distinction may be formalized by defining a reference elevation (pycnocline) and using, e.g., a Fourier filter for examining its frequency content. We define the pycnocline here using the density gradient as a weight function,

$$h_L(t) = \frac{1}{\int_0^h \left|\frac{\partial \rho}{\partial z}\right| dz} \int_0^h z \left|\frac{\partial \rho}{\partial z}\right|^n dz, \tag{24}$$

where h_L is the elevation (or thickness of the lower layer) at the sensor location. The pycnocline elevation generally differs from the local N^2 maximum; the power is used as a device to shift it toward the maximum gradient when it dominates (here, $n = 2$). Filtering out oscillations shorter than 5 min, corresponding, e.g., to wind and infragravity waves, equation (24) produces the black line in figures 2–3. The red curve retains only oscillations longer than 1 hr. Note that the pycnocline elevation agrees well with the local N^2 maximum during organized internal wave events.

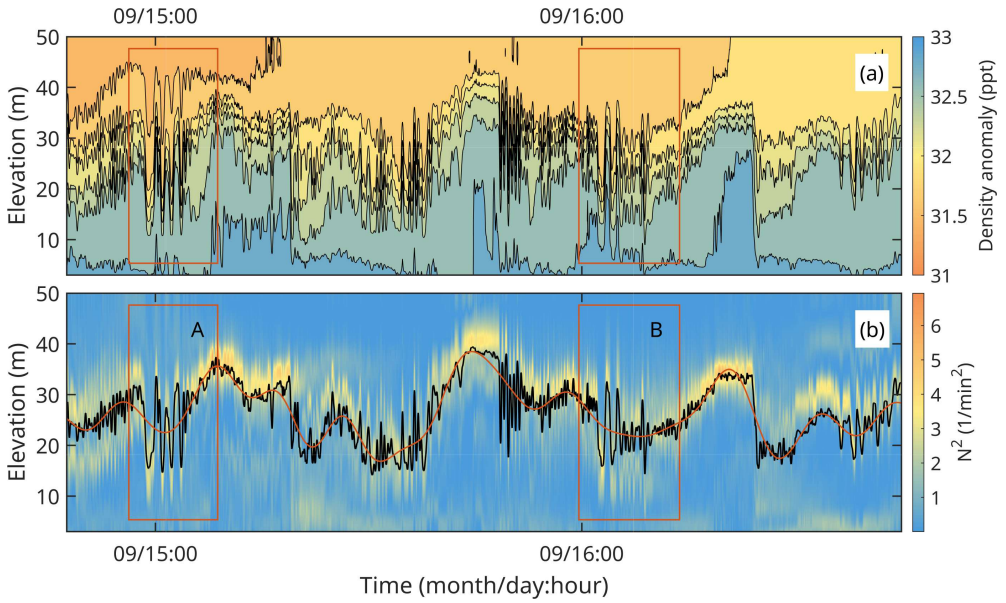


Fig. 2: Analysis of observed density stratification at the NRL50N station, 50-m isobath. Vertical structure of a) density anomaly ($\rho - 10^3$ kg/m^3), and b) N^2 (equation 6). In panel (b) the black line marks the pycnocline elevation estimated using the two layer stratification; the red line represents the baroclinic tide component of the pycnocline, estimated using a Fourier low pass filter (see text for detail). Rectangles marked *A* and *B* represent two events discussed in detail below.

The discussion below focuses on two internal wave events, marked by red rectangles, denoted *A* and *B*. Wave groups at 50-m and 35-m observation are identified as the same event approximately: for a propagation distance of ≈4 km, using a characteristic long wave speed $c_0 = \sqrt{\frac{g' h_U h_L}{h}} \approx 0.4$ m/s yields a time lag ≈2.8 hr. Figures 4–5 show the two wave groups in more detail. The evolution of the internal wave groups *A* and *B* from the 50-m to the 35-m isobaths is significant, and significantly different, despite similar initial appearance. Both wave groups show elements of nonlinear evolution: group *A* has a sinusoidal appearance, but the number of waves is not conserved by the evolution between the two sites (figure 4, compare panels a and c). The waves in group *B* develop sharp peaks and flat troughs, similar to cnoidal waves, or solitons of elevation (figure 5a and c). These characteristics of wave groups *A* and *B* are an important test for the flow reconstruction method described above, which does not account for wave nonlinearity.

Wave nonlinearity may be estimated using a simple two-layer model based on the Gardner equation (see appendix B). The scaled equation defines two Ursell numbers, $s_{2,3}\sigma^2_{2,3}$, that compare the quadratic and cubic nonlinear terms (hence the indices) to the dispersive term. Over the duration of wave group *A*, the background pycnocline depth $h_U = h - h_L$ (dark red line in figures 4–5) varies between 19.7 m and 28.4 m at the 50-m station, and between 18.6 m and 24.6 m at the 35-m station (table 1). For wave packet *A*, the quadratic Ursell number changes sign over its time span, which suggests that quadratic nonlinearity is overall weak

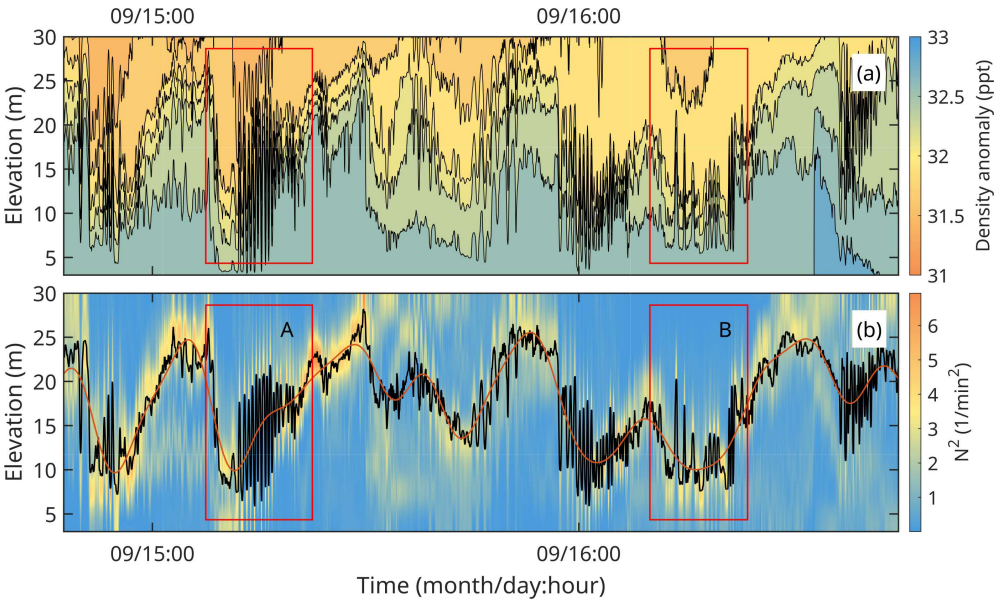


Fig. 3: Analysis of observed density stratification at the NRL35N station, 35-m isobath. Same organization as in figure 2. The arrival time of events *A* and *B* with respect to the 50-m station lags on average by ≈ 3.5 hr.

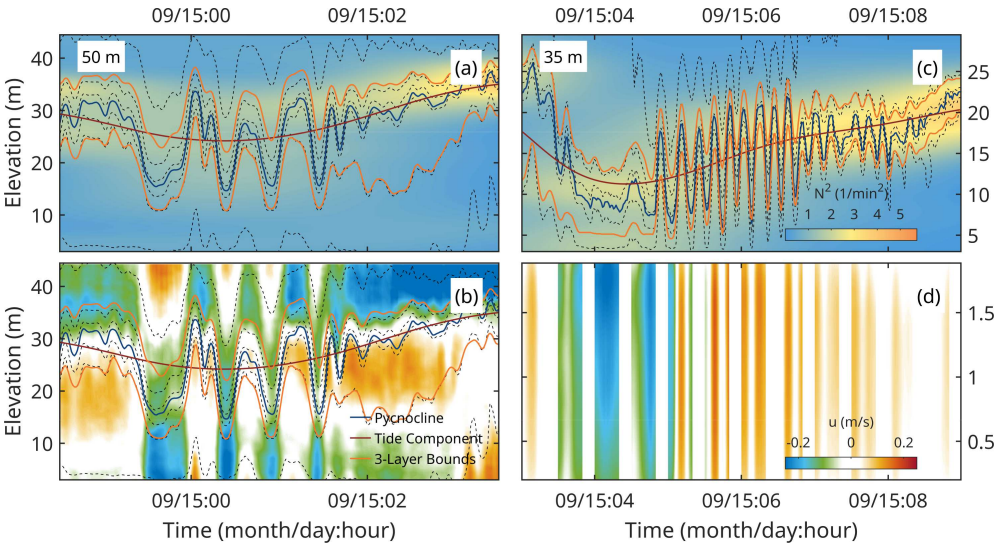


Fig. 4: Details of the stratification and flow velocity during event *A*; left: 50-m station, right: 35-m station. Vertical structure of a,c) N^2, and b,d) horizontal velocity, east component. Blue and red lines: elevation of the pycnocline and three-layer boundaries, respectively. Note the different vertical range of panels (b) and (d).

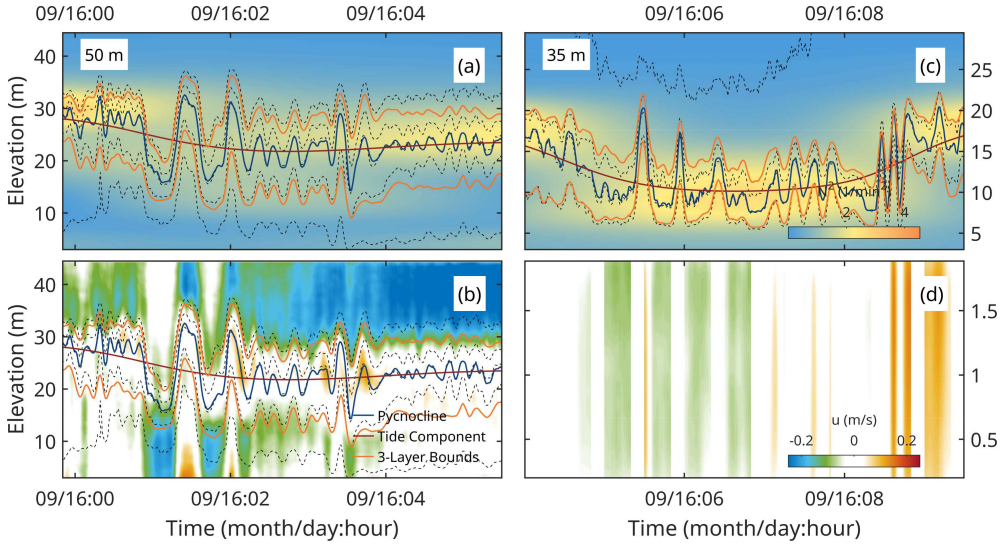


Fig. 5: Details of the stratification and flow velocity during event *B*; left: 50-m station, right: 35-m station. Vertical structure of a,c) N^2, and b,d) horizontal velocity, east component. Blue and red lines: elevation of the pycnocline and three-layer boundaries, respectively. Note the different vertical range of panels (b) and (d).

– which may explain the sinusoidal aspect of the waves at 35-m. In contrast, the quadratic nonlinearity of wave packet *B* is positive at the 35-m station, consistent with the wave aspect of solitons of elevation. This evolution highlights the role of the internal tide phase in the evolution of internal waves.

Event	h(m)	h_U(m)	a(m)	T(min)	$s_2\sigma_2^2$	$s_3\sigma_3^2$
A	50	[19.7, 28.4]	8.5	30.3	$[-846, 534]$	$[-1{,}400, -1{,}350]$
A	35	[18.6, 24.6]	6.1	13.9	$[-136, 550]$	$[-531, -419]$
B	50	[23.7, 27.2]	8.2	36.22	$[-265, 474]$	$[-1{,}760, -1{,}740]$
B	35	[21, 25.12]	5.6	18	$[380, 979]$	$[-804, -620]$

Table 1: Characteristic scales and coefficients of equation (B11) for internal waves during events *A* and *B*; h is the water depth; h_U is the pycnocline depth, dark red line in figures 2–3; a and T are the characteristic amplitude and period of the internal wave group; $\sigma_{2,3}^2$ are the magnitudes of the quadratic and cubic Ursell numbers, and $s_{2,3} = \pm 1$. Due to tidal modulation, the value of h_U spans the interval, and consequently so do the Ursell numbers. The interval limits are given in square brackets.

For the two events selected here, velocity measurements (figures 4–5, lower panels) contain a strong internal wave component, but show significant tidal flows outside the group time

span. Note that the 35-m array recorded flow in only up to 1.8 m above the seabed. Because the velocity measurements were collected in bursts, some internal wave crests were not captured.

3.2 Application of the flow reconstruction approach

Here, we apply the flow reconstruction approach discussed above to events *A* and *B*, following the steps outlined in section 2.2. Recall that the goal of this procedure is to reconstruct the flow induced by internal waves. The tidal component of the stratification is assumed to define the background state, e.g., $\overline{\rho}$, while internal waves define the perturbation $\widetilde{\rho}$. All measured quantities were separated into background and perturbation components using a Fourier filter: internal waves (perturbation) were identified as oscillations with periods between 5 min and 1 hr, with tidal oscillations (background) having periods >1 hr. Wind and infragravity waves (periods in the order of 10 s and 1 min, respectively) were filtered out.

Temperature profiles were smoothed and interpolated using a cubic spline, and resampled to a smaller vertical bin size of 0.2 m. The salinity measurements collected at NRL35N ranged between 33.33 ppt and 33.56 ppt; a constant salinity of 33.5 ppt was chosen for all temperature moorings. The density of the seawater was calculated using the equation of state for ocean salt water (Millero and Poisson, 1981) assuming the atmospheric pressure is equal to 1 bar.

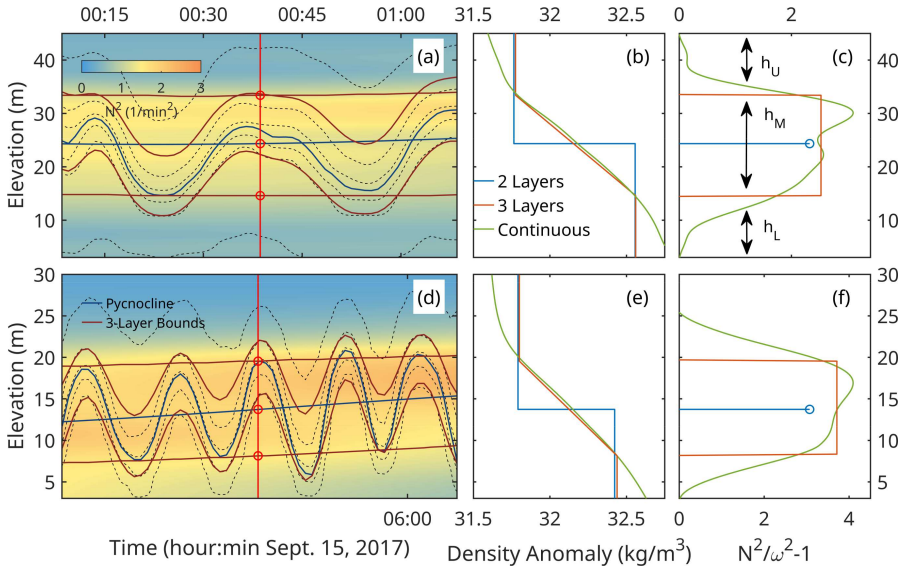


Fig. 6: Observed stratification and simplified models for event *A* at the two stations: 50-m, top; and 35-m, bottom. a,d) A 1-hr time window used in the windowed Fourier transform analysis, showing the vertical structure of N^2 with pycnocline (dark blue) and boundaries of the three-layer model (equation 20). The smooth, almost straight lines represent the background. b,e) profile of the density anomaly and two- and three-layer models for the center point of the window, marked by a bright red line in panels (a,d). c,f) Weight function of the Sturm-Liouville equation (11) corresponding to the continuous, two- and three-layer models of the stratification.

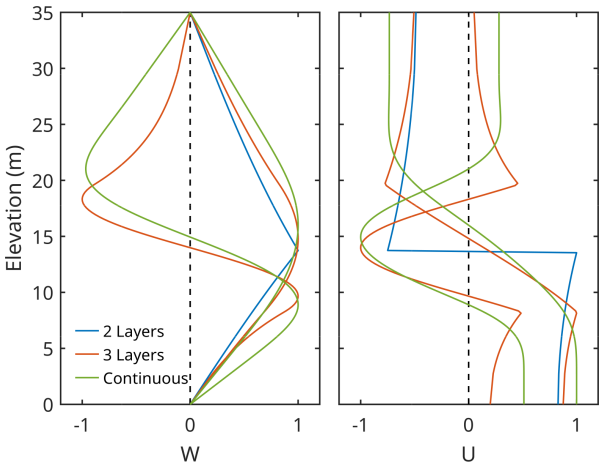


Fig. 7: Vertical modes of Sturm-Liouville problem (11-12), computed for the 15-min Fourier component, event *A*, stratification at 35-m site shown in figure 6: a) vertical velocity W; b) east component U of horizontal velocity. For clarity, only the first two modes are shown; they may be distinguished by the number of zero crossings: first mode has no zero crossing for W, and one for U. The two layer model has only the first vertical mode.

For the two layer approximation, the thickness h_L of the lower layer was estimated using equation (24); for the three layer approximation, the layer thicknesses $h_{L,M,U}$ were estimated as

$$\overline{\rho}\,(z \le h_L, t) \ge 0.75\,\Delta\overline{\rho}(t), \quad \text{and} \quad \overline{\rho}\,(z > h_L + h_M, t) \le 0.25\,\Delta\overline{\rho}(t) \tag{25}$$

where $\Delta\overline{\rho}(t) = \overline{\rho}\,(0,t) - \overline{\rho}\,(h,t)$. The background velocity was ignored.

At Point Sal latitude (34.9021013°N), the Coriolis factor $f = 0.832 \times 10^{-4}$ rad/s, comparable to the characteristic inertial period 20.97 hr, and with the frequency of the diurnal component of the internal tide, but approximately two orders of magnitude smaller than internal wave frequency. Coriolis terms were therefore neglected.

At the 50 m station, the vertical average of the wave velocity components direction was approximately 10° clockwise from the east direction for both *A* and *B* events. Because the model used here primitively reconstructs the flow velocity in the direction of propagation, to compare with observations the propagation angle was estimated at each elevation level using a linear fit to the (u,v) hodograph in time sliding 60-min windows. The resulting angle was smoothed using a cubic spline. At the 35-m station, the direction was aligned with the east axis within less than 1° error, therefore the observed east velocity component was used for comparison.

To account for the variation of the background stratification induced by slow tidal oscillations, the linear model was implemented using a windowed Fourier transform. Time series were divided into 60-min windows at 0.8 overlap. The results below were obtained using three stratification models: the two- and three-layer models, and the measured stratification, referred to below as "continuous". The Sturm-Liouville problem (11-12) was solved for the

modal structures (first three modes) for each time window, using a shooting algorithm for the continuous stratification. Modal amplitudes α_n (equation 15) were calculated from the reference quantity, either B or Z (see section 2.2). The vertical structure of the other flow quantities were then obtained via the transfer functions (8). The resulting time series were obtained using the inverse windowed Fourier transform. All calculations were performed using MATLAB®.

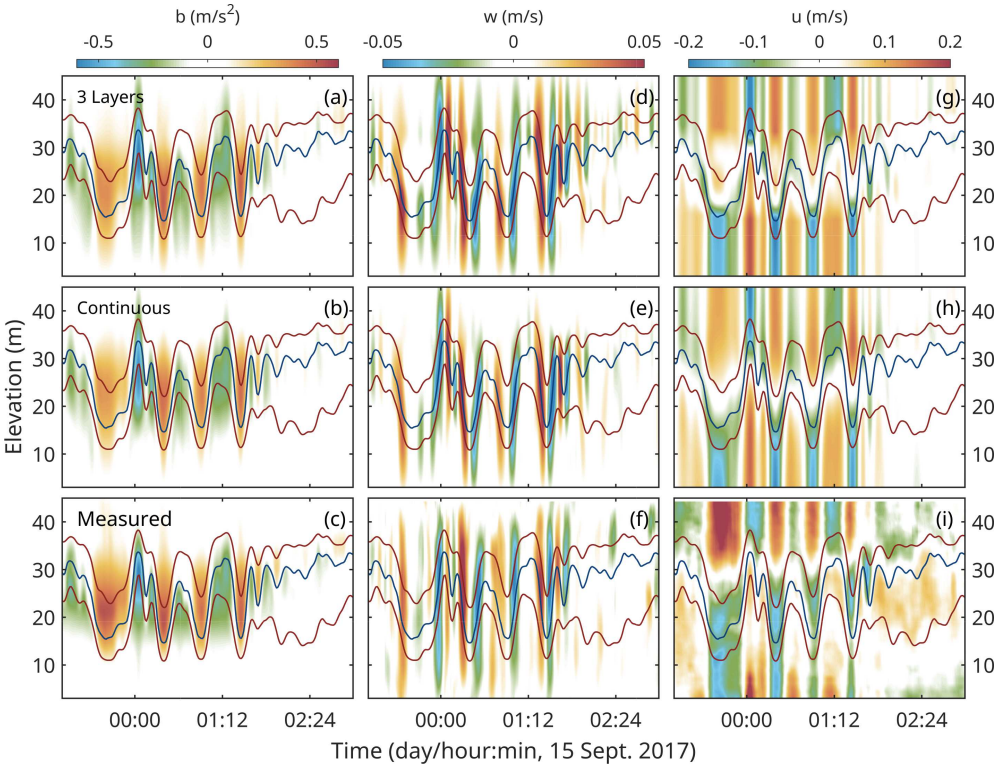


Fig. 8: Flow reconstruction, global method (see section 2.2) for event A at the 50-m station (see figures 2-4): buoyancy (a-c); vertical velocity (d-f); horizontal velocity (g-i). Panel rows: top – three-layer model; middle – continuous stratification; bottom – observations. Note that because the reconstruction provides the horizontal velocity along the direction of propagation, the observations combine the east and north velocity components.

Figures 6–7 show an example of the vertical structure calculation for event A. For every time window, the stratification was approximated by the vertical structure of $\overline{\rho}$ at the center point (vertical red line, figure 6a,d, green lines in figure 6b,c,e,f). The three-layer model was constructed based on equation (25); for the two-layer model, the interface was defined by the tidal component of the pycnocline (equation (24); figure 6b,c,e,f; see figures 4–5). Examples of the vertical structures of the vertical velocity and horizontal velocity for the first two modes (one mode for the two-layer model) are shown in figure 7.

To avoid noise due to small-number divisions due to the intermittent character of the internal wave signal, the deviation of the reconstructed quantities from observations is measured here by a mean square distance applied to the vertical structure of the quantity normalized by the maximum absolute value, e.g.,

$$\delta_u = \frac{\sqrt{\sum_z \left[u^2_{obs}(z,t) - u^2(z,t)\right]}}{\max_{z,t}\left(|u_{obs}(z,t)|\right)}, \tag{26}$$

where the indices of the $\sum$ and max operators indicate the range of application.

3.3 Results

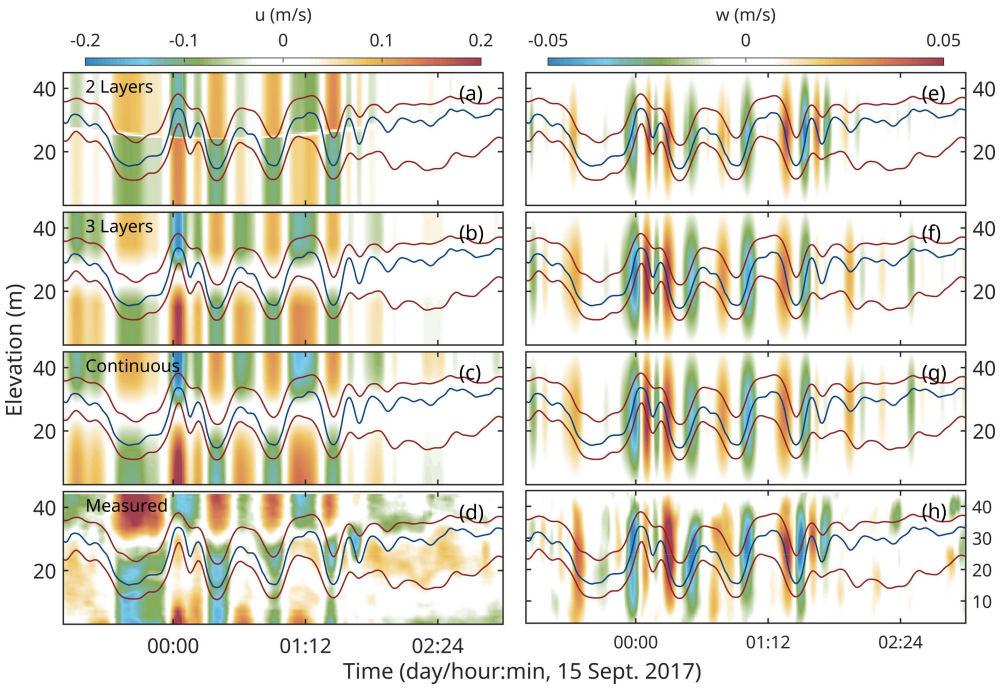


Fig. 9: Flow reconstruction, local method (see section 2.2) for event *A* at the 50-m station (see figures 2-4): horizontal velocity (a-d); vertical velocity (e-h). Panel rows, top to bottom: two layer stratification model; three-layer stratification model; continuous stratification; observations.

The results of the reconstruction applied to events *A* and *B* are summarized in Figures (8-11).

The observations at the 50-m array include the vertical structure of both stratification and flow, allowing for an examination of the full reconstructed flow. Figure 8 compares observed

buoyancy and velocity to the global reconstruction using the three-layer and continuous models (equation 17), with the first three vertical modes. At visual inspection, both versions of the linear model reproduce fairly well the buoyancy estimated from observations (figure 8a-c), which suggests that the estimated elevation of the three layers (also pycnocline, see below the local estimates) is adequate. The reconstructed vertical and horizontal velocity fields also reproduce well the internal wave pattern of the observations, but deviate from observations in some details; for example, the reconstructed components have a more uniform vertical structure than the measurements (expected, see figure 7). For the duration of the internal wave group, excluding the initial wide trough, the reconstruction reproduces the observed buoyancy with an integral deviation measure (equation 26) of overall < 0.05 for the three-layer model and < 0.025 for the continuous model (figure 10b). The horizontal velocity deviation is overall < 0.10 (figure 10c).

The local reconstruction approach, figure 9 produces remarkably similar results, with a similar deviation measure (figure 10d). The agreement between the global and local models is consistent with the magnitudes of the modal buoyancy amplitudes: $\beta_0 \approx 2.5\beta_1$ for much of the duration of the wave group (figure 11b). Despite the relatively adequate representation of the observed buoyancy, a notable systematic disagreement between the reconstructed and measured velocity is the elevation of the zero-velocity layer, which is ≈ 5 m lower in the reconstructed velocity (compare panels g-h with f in figure 8; panels a-c with d in figure 9). As the stratification models capture well the buoyancy distribution, the source of the disagreement must be a barotropic process, not covered by the model – this discrepancy is examined quantitatively in section 4. Reconstruction results for event *B* exhibit very similar features (showing only the global reconstruction in figure 12), but in this case the zero-velocity layer matches the observations.

Observations at the 35-m station provide the full vertical structure of the stratification, therefore allowing for both the global and local methods, with buoyancy reconstruction results similar to the 50-m results (not shown). However, detailed velocity measurements are available only in the first 1.8 m above the bed (figures 4- 5, panel d), most of which lies within the bottom boundary layer, which reduces the options for meaningful comparisons to measurement points near 1 m above seabed (figure 13). Because the burst measurements often missed wave crests or troughs, a consistent deviation measure cannot be applied, especially for short wave groups. Still, the identifiable reconstruction features suggest a similar performance as at the 50-m site. Global and local reconstruction methods are again very similar. The first mode is even more dominant (figure 11d). The reconstruction gives a qualitatively similar result for both events *A* and *B*, despite the latter being demonstrably more nonlinear (table 1) – we return to why the linear method is nonetheless robust to this nonlinearity in section 4.

4 Summary and discussion

In this study, we use a linear model to reconstruct flow from stratification (information which may be obtained remotely). Although the ability of reconstructing the flow on an ocean shelf from remote measurements of stratification has important applications in understanding the dynamics of internal waves, to our knowledge this study is the first to attempt such a reconstruction. Because the limitations of such a reconstruction are not fully understood, our approach focuses on internal waves, defined here as baroclinic perturbations with temporal

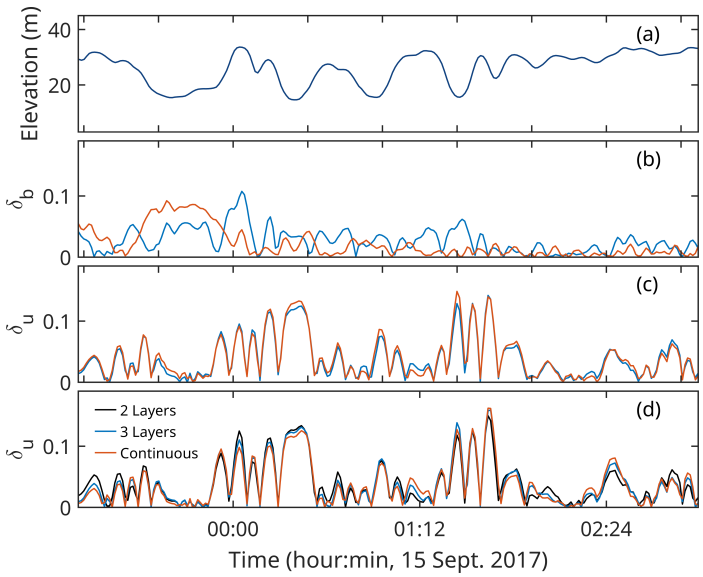


Fig. 10: Deviation of the reconstructed quantities from observations (equation 26) for event *A* at the 50-m station: a) pycnocline elevation, provided as time reference; b) buoyancy; c) horizontal velocity, global method; d) horizontal velocity, local method.

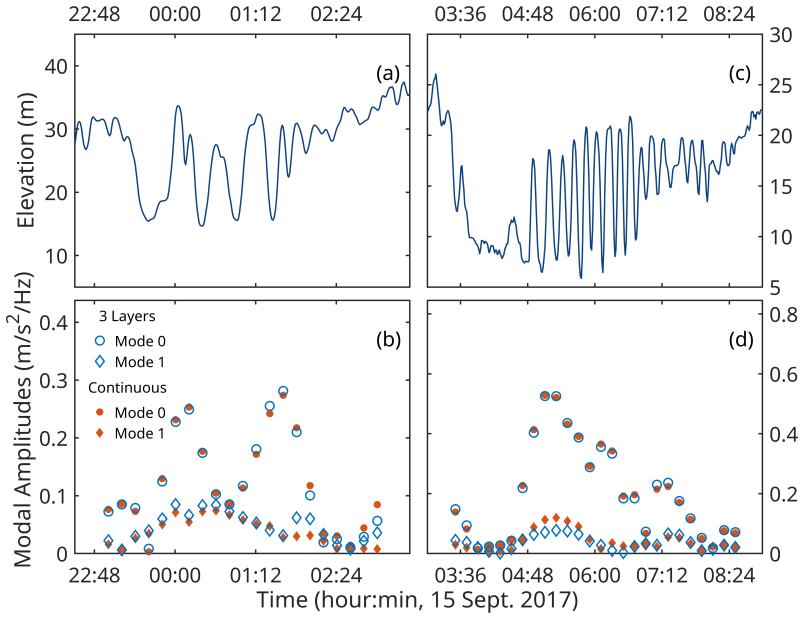


Fig. 11: Amplitudes of the first two vertical modes of the buoyancy (β_n in equation 17), for the 15-min Fourier component; at 50-m, left, and 35-m, right. a-c) Pycnocline elevation (for time reference). b-d) Modal amplitudes.

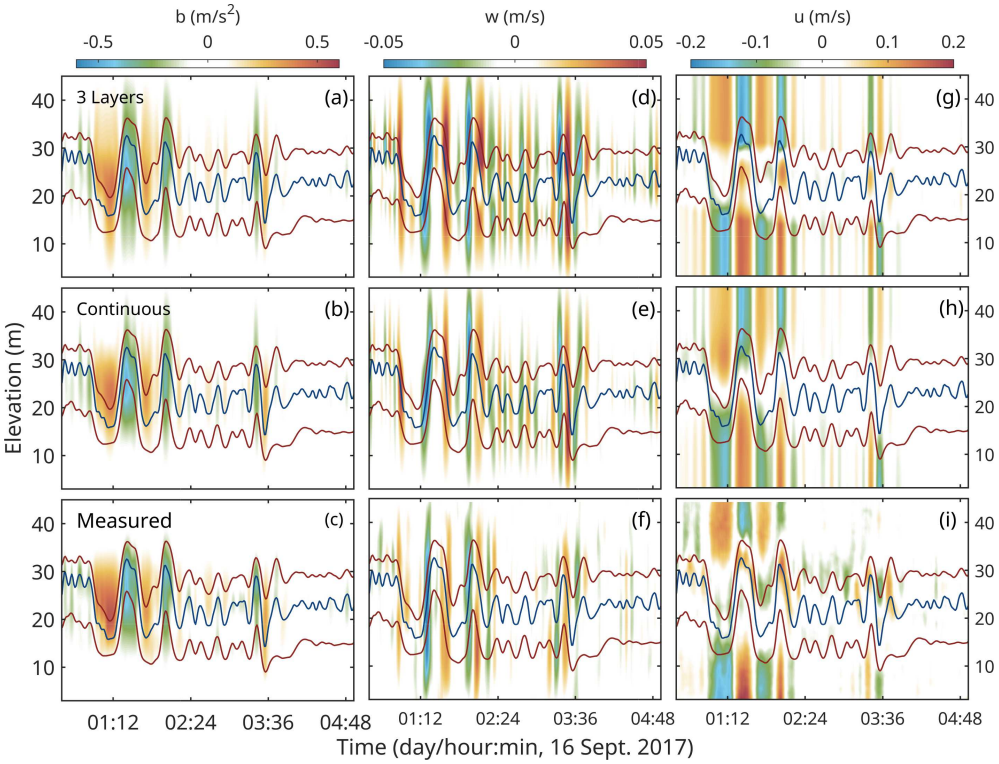


Fig. 12: Flow reconstruction, global method (see section 2.2) for event *B* at the 50-m station (see figures 2-4): buoyancy (a-c); vertical velocity (d-f); horizontal velocity (g-i). Panel rows: top – three-layer model; middle – continuous stratification; bottom – observations.

scales in the order of a few tens of minutes. The field observations used here, two moorings deployed near the 50 and 35-m isobath, approximately 4 km apart, provide resolution information about the time evolution of the local stratification and flow field.

The reconstruction method is built on a few assumptions: the basic existence and measurability of the background stratification and its perturbations; and additional simplifying assumptions – linearity, negligible background flows, various simplified stratification models, and others. The basic condition requires that stratification provides enough information to attempt to retrieve information regarding the baroclinic flows. The limitations introduced by the simplifying assumptions may in principle be removed by using a more complicated model, but from the point of view of practical applications, it is useful to consider the viability of the simplest model.

The discussion presented here is limited to small scale baroclinic flows (internal waves), suitable for testing using local mooring observations. We do not attempt to describe large scale processes such as wind circulation, barotropic and baroclinic tides, etc., whose generation, propagation direction, and interaction involve a large spatial domain not covered by our local observations.

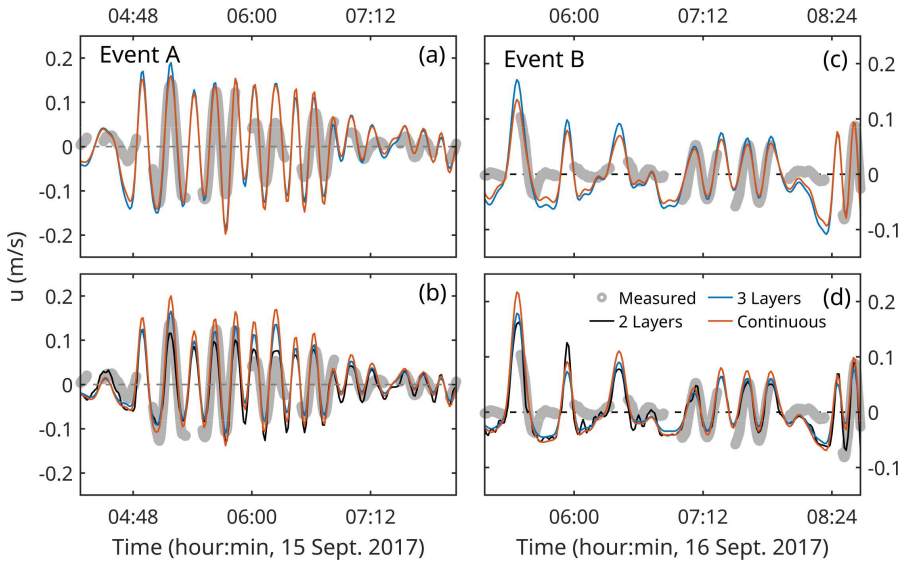


Fig. 13: Reconstruction of horizontal velocity component for events *A* (left) and *B* (right) at the 35-m station, at 1-m above the bed. At this location the direction of wave propagation was eastward. a,c) Global method (see section 2.2). b,d) local method.

4.1 Internal wave nonlinearity

The observations show that the evolution of wave group *A* is significantly nonlinear (number of crests is not conserved), but at the 35-m array the group appears to be near a polarity change (vanishing quadratic nonlinearity), which may explain the rather linear, sinusoidal aspect. Wave group *B* is also nonlinear, with cnoidal-like sharp peaks and flatter troughs. However, our linear reconstruction method appears to agree well enough with observations. There are two reasons for this. First, although the Ursell numbers $\sigma^2_{2,3}$ are significant, they are derived in a dynamical, global context, in which local effects might still be small. More importantly, the effect of the nonlinearity is to generate bound components that do not obey the linear dispersion relation and are phase coupled to the linear Fourier modes. Our method, however, transfers this phase coupling from the observed variable (either $\widetilde{b}$ or ζ) to the reconstructed quantities, so the error introduced by enforcing the linear dispersion is comparably much smaller. The results suggest that not accounting for nonlinearity in *local* flow reconstruction applications is not critical if waves do not break (breaking would also invalidate the method by destroying the stratification, negating the fundamental condition of the method).

4.2 Role of large scale processes

Including background flow effects poses a more difficult problem. The effect of baroclinic background flows on stratification is partially accounted for in the background quantities by using filters to separate scales, and windowed Fourier transform (e.g., the "tide component" of the pycnocline, figures 4-5). The direction of propagation is, however, impossible to establish from local measurements alone. In addition, barotropic components, such as barotropic tides

and wind driven currents, do not produce detectable perturbation in stratification, and therefore cannot be identified from the stratification alone. To determine their contribution to the background flow requires additional, large scale information, such as the effect of a nearby coast and its alongshore structure, atmospheric flows and events, etc. This changes altogether the scope and difficulty of the problem.

While these processes were neglected in the reconstruction itself, they are present in the observations and cause a detectable effect. In section 3.3 we noted the discrepancy of the zero-flow layer elevation between observed and reconstructed horizontal velocity structures (≈5 m, e.g., figure 8g-i) during event *A* at the 50-m station – a discrepancy that is absent for event *B* at the same station. Figure 14c shows that at the 50-m site, the background flow for wave group *A* has a strong south component, ≈ 0.1 m/s immediately above the pycnocline. This appears to cause a significant rotation in the superposed internal waves: oscillations have a prominent north component above the pycnocline, but shift to an east component only below. The position of the background shear layer is consistent with the elevation of the zero-velocity layer seen in figure 8g-i. These background flow features cannot be derived from the stratification alone (e.g., pycnocline in figure 4).

To assess whether the wind forcing preceding each event is consistent with a locally formed, wind-driven Ekman layer, we examined 10-min wind observations from NDBC buoy 46011, the station nearest Point Sal, over the 24 hr (≈ inertial period 20.97 hr) preceding each event onset (≈00:01, 15 September for event *A*; ≈01:50, 16 September for event *B*). Over this window, event *A* shows a pronounced diurnal reversal: wind direction is highly variable (standard deviation ≈ 81°) and speed drops intermittently below 1.5 m/s for roughly 6 hr around midday on 14 September, before reorganizing to a steady northwesterly flow only in the final ∼6 hr of the window. The resulting 24-hr vector-mean wind stress is correspondingly weak and inconclusive for the Ekman layer formation. Event B, by contrast, is forced by a wind that is steady in direction (standard deviation ≈ 7°) and strong (6–11 m/s) throughout the full 24-hr window, which is a record well suited, in principle, to the formation of an equilibrium Ekman layer.

Wind stress was computed using the bulk formula of Large and Pond (1981), $\tau_0 = \rho_a C_D(U_{10}) U_{10}^2$, $C_D(U_{10}) = (0.75 + 0.067 U_{10}) \times 10^{-3}$, vector-averaged over each 24-hr window: $\tau_0 \approx 0.009$ Pa for event *A* ($\overline{U}_{10} \approx 2.7$ m/s) and $\tau_0 \approx 0.124$ Pa for event *B* ($\overline{U}_{10} \approx 8.6$ m/s), a factor of ∼14 difference for the computed wind stress, consistent with the contrast in wind character noted above.

The relevant comparison is the wind-driven current at the depth where the reconstructed/observed offset actually occurs, not at a shallow, near-surface depth: the pycnocline elevation for event *A* spans 19.7–28.4 m (table 1), i.e. 22–30 m below the sea surface at this 50-m station. We evaluate the classical Ekman spiral

$$D_E = \sqrt{\frac{2A_z}{f}}, \qquad V_0 = \frac{\tau_0}{\rho_0 \sqrt{A_z f}}, \qquad V(z_d) = V_0\, e^{-z_d/D_E}, \tag{27}$$

at $z_d = 20$–30 m, for two regimes of eddy viscosity: a weakly-turbulent, stratified-pycnocline interior, vertical eddy viscosity $A_z = 10^{-4}$–$10^{-3}\,\mathrm{m^2/s}$ (e.g., Gregg, 1989), and a strongly-mixed (effectively unstratified) water column, $A_z = 10^{-2}$–$10^{-1}\,\mathrm{m^2/s}$. For the stratified-interior regime, $D_E \approx 1.5$–5 m for both events: the wind-driven layer does not reach the

pycnocline at all, i.e. $V(z_d) \approx 0$ regardless of wind strength. For the strongly mixed regime, $D_E \approx 15.5$–49 m, and the wind signal reaches 20–30 m with $V(z_d) \approx 0.14$–0.26 cm/s for event A and ≈ 1.9–3.6 cm/s for event B.

Neither regime supports a wind-Ekman explanation of the observed ≈10 cm/s south-component background flow. The strongly mixed regime is, moreover, not a physically admissible description of this site: the thermistor record shows strong, persistent stratification at the pycnocline depth throughout both events (figures 2–6), which is incompatible with an eddy viscosity large enough to homogenize momentum over that depth range. It quickly becomes clear that a local, wind-driven Ekman mechanism is not a viable stand-alone explanation for the offset at either site.

Beyond the present bulk estimate, the barotropic tide component itself could in principle be supplied directly rather than inferred: regional barotropic tide inversions such as OTIS/OTPS (Egbert et al., 1994; Egbert and Erofeeva, 2002) assimilate satellite altimetry and tide gauge records into a shallow-water circulation model to produce depth-averaged tidal currents at any coastal location, including Point Sal, independent of any local stratification measurement. Adding the OTIS-predicted barotropic current to the present reconstruction and comparing against the observed 50-m velocity would show whether the offset diminishes, implicating the barotropic tide, or persists, pointing instead to a non-local wind-driven circulation. We have not implemented this here: it requires extracting and predicting the relevant tidal constituents at Point Sal from an appropriate regional grid; a persistent residual would need to be interpreted with care rather than taken simply as a failure of the tidal prediction. This is a substantive addition to the analysis rather than a back-of-envelope check, and we leave it for future work rather than undertake it within the scope of the present revision.

We conclude that in any real application, background flows are expected to be important and should be considered, perhaps estimated using additional observational data (e.g., circulation models, satellite information, weather predictions).

Event	h(m)	$\overline{h}_U$(m)	a (m)	T(min)	$s_2\sigma_2^2$	$s_3\sigma_3^2$
A/*B*	50	19.7	6.7	720	-3.8×10^5	-4.9×10^5
A/*B*	35	15.6	5.4	720	-3.1×10^5	-8.8×10^5

Table 2: Characteristic scales and coefficients of equation (B11) for internal tides during events A and B; h is the water depth; $\overline{h}_U$ is the pycnocline depth, the time average of the dark red line in figures 2-3; a and T are the characteristic amplitude and period of the internal tide; $\sigma^2_{2,3}$ are the magnitudes of the quadratic and cubic Ursell numbers, and $s_{2,3} = \pm 1$.

We also note briefly that, at least on the shallow inner shelf at Point Sal, CA, the baroclinic tide is strongly nonlinear, and likely cannot be modeled using a linear model. Table 2 shows the corresponding Ursell numbers, estimated as for the internal waves using the Gardner equation (B11). Both Ursell numbers have very large values, indicating that the tide evolves as a Riemann wave; the quadratic and cubic nonlinear terms are negative, $s_{1,2} = -1$, indicating that the tide behaves as a nonlinear wave of depression.

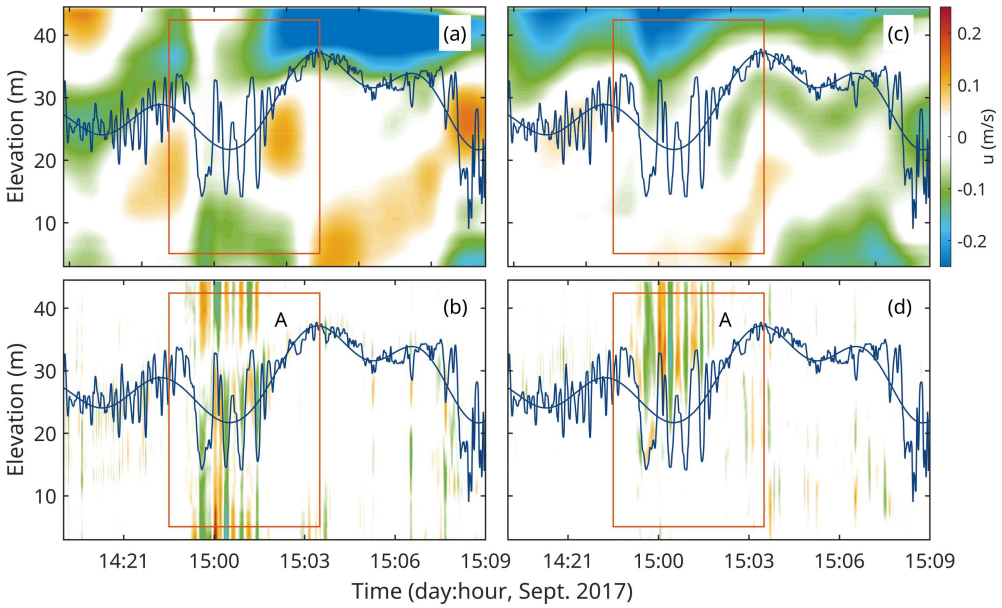


Fig. 14: Overview of the scale decomposition of the flow velocity measurements at 50-m, obtained using a Fourier filter (east component – left; north component – right). a,c) Large scale flows, corresponding to periods >1 hr. b,d) internal waves, periods <1 hr. Periods <5 min, for example, due to surface infragravity and wind waves, have been filtered out. Dark blue lines mark the pycnocline derived from the density estimates. Event *A* is marked by a red rectangle.

5 Conclusions

Our results suggest that it is possible to retrieve a credible flow field from stratification in a well-stratified shelf environment, at least for internal waves, using relatively simple means: a linear model and some information about the stratification, even limited to the pycnocline. We find that the observed horizontal velocity field is reproduced with overall error less than 10% by using just the first vertical mode of a multilayer (>2) model. The method presented here has two important limitations: it obviously does not work for strongly mixed environments, and may be significantly affected by strong large scale processes, such as barotropic tides and wind generated currents, which may not have a detectable effect on the stratification – an effect for which we provide, in section 4.2, an order-of-magnitude quantitative argument consistent with the observed ≈5-m zero-velocity-layer offset at the 50-m station. Further improvement of the results can be expected if more sophisticated models and methods that include the effect of larger scale flows are employed.

Acknowledgements. This paper is dedicated to the memory of Prof. V. I. Shrira, a generous mentor and dear friend, who passed away during the manusript preparation. An external member of R. Qayyum's doctoral committee with extensive experience in nonlinear wave dynamics on continental shelves, he guided much of the analysis and contributed key corrections throughout.

This work formed part of R. Qayyum's doctoral dissertation. A. Sheremet chaired the dissertation committee and motivated the study; J. Calantoni and J. Simeonov, both of the Naval Research Laboratory, also served on the committee and provided valuable support and assistance.

Declarations

Author contributions. A.S. conceived the study. R.Q. and A.S. carried out the mathematical modeling and prepared the figures. A.S. provided the physical interpretation of the results, critically evaluated the analysis, and contributed key corrections throughout. All authors contributed equally towards writing the manuscript.

Funding. A. S and R. Q were partially supported through the NRL BAA N00173-21-2-C900. The authors thank members of the Office of Naval Research (ONR) for the technical support in planning and executing field experiments.

Data availability. The data used in this study was collected during the 2017 Inner Shelf Dynamics Experiment. The data is stored in the repository managed by the UCSD Library Digital Collections (Waterhouse et al., 2020).

Ethics. Not applicable.

Competing interests. The authors declare no competing interests.

Consent for publication. Not applicable.

Financial interests. The authors have no relevant financial or non-financial interests to disclose.

Appendix A Piecewise linear stratification models

A.1 Three layers

The three layer stratification model (equation 20) is used in this study only for internal waves. Therefore, in equation (11) we neglect the Coriolis terms and assume that the waves propagate toward the east, i.e., $k_x = k$. The equation is solved with boundary conditions (12) and assuming continuity of the velocity field at the interfaces $z = h_L$ and $z = h_L + h_M$,

$$\lim_{z \nearrow h_L} \begin{pmatrix} W \\ W_z \end{pmatrix} = \lim_{z \searrow h_L} \begin{pmatrix} W \\ W_z \end{pmatrix}, \quad \text{and} \quad \lim_{z \nearrow h_L + h_M} \begin{pmatrix} W \\ W_z \end{pmatrix} = \lim_{z \searrow h_L + h_M} \begin{pmatrix} W \\ W_z \end{pmatrix}. \tag{A1}$$

With the stratification given by equation (20) the solution is

$$W(z) = A \begin{cases} \sin(\kappa h_L + \varphi) \dfrac{\sinh kz}{\sinh kh_L}, & 0 \le z \le h_L \\ \sin(\kappa z + \varphi), & h_L \le z \le h_L + h_M \\ \sin[\kappa(h_L + h_M) + \varphi] \dfrac{\sinh k(h - z)}{\sinh kh_U}, & h_L + h_M < z \le h \end{cases} \tag{A2}$$

with

$$\tan(\kappa h_L + \varphi) = \frac{\kappa}{k}\tanh(k h_L). \tag{A3}$$

and the horizontal and vertical wavenumbers k and κ satisfy the dispersion relation

$$\kappa^2 = k^2\left(\frac{N_M^2}{\omega^2} - 1\right), \tag{A4}$$

together with the solvability condition

$$\tan \kappa h_M = \frac{\kappa k \sinh k(h_L + h_U)}{\kappa^2 \sinh k h_L \sinh k h_U - k^2 \cosh k h_L \cosh k h_U}. \tag{A5}$$

In the three-layer case, the three parameters ω, k, κ are subject to two functional constraints, the dispersion relation (A4) and the solvability condition (A5), therefore one of the parameters is free. Because frequency is an invariant of the shoaling process, a natural choice is to let ω be the free parameter, while k and κ are determined by equations (A4) and (A5).

A.2 Two layers

The two layer model is a degenerate case of the three layer model for $\Delta = 0$, with $N = 0$ in the entire fluid body, which implies that $b = 0$ and $\rho = 0$. Neglecting the Coriolis factor f, equation (11) becomes

$$W_{zz} - k^2 W = 0. \tag{A6}$$

With continuity conditions for W at the interface

$$\lim_{z \nearrow h_L} W = \lim_{z \searrow h_L} W \tag{A7}$$

the solution takes the form

$$W(z,\omega) = A \begin{cases} \frac{\sinh kz}{\sinh k h_L} & z < h_L \\ \frac{\sinh k(h-z)}{\sinh k h_U} & z > h_L \end{cases}$$

where A is the amplitude of the displacement of the interface, and k satisfies the dispersion relation

$$\omega^2 = \frac{gk(\rho_L - \rho_U)}{\rho_U \coth k h_U + \rho_L \coth k h_L}$$

which may be simplified using the Boussinesq approximation $2\rho_{U,L}/(\rho_L + \rho_U) \approx 1$ to

$$k(\omega) = \frac{\omega^2}{g'}\left[\coth k(h - h_L) + \coth k h_L\right], \text{ with } g' = 2g\frac{\rho_L - \rho_U}{\rho_L + \rho_U}.$$

Appendix B Wave nonlinearity

The nonlinear character of the pycnocline oscillations (internal tides and waves) is estimated using the rotational Gardner equation, which has been shown to capture well the nonlinear

dynamics of long pycnocline perturbations (Pelinovsky et al., 1994; Holloway et al., 1999; Holloway, 2001; Helfrich and Melville, 2006; Grimshaw et al., 2010). The Gardner equation (e.g., Gardner et al., 1967; Slyunyaev and Pelinovski, 1999; Kamchatnov et al., 2012) may be regarded as an extension of the Korteweg–de Vries (KdV) equation that includes cubic nonlinearity. In a two layer stratified fluid, the Gardner equation for internal waves (Helfrich and Melville, 2006) on the pycnocline is

$$\eta_t + c_0\left(1+\alpha_1\eta+\alpha_2\eta^2\right)\eta_x + c_0\beta\eta_{xxx} = 0 \tag{B8}$$

with coefficients

$$\alpha_1 = \frac{3}{2}\frac{\Delta h}{h_U h_L};\ \beta = \frac{1}{6}h_U h_L;\ \alpha_2 = \frac{3}{\left(h_U h_L\right)^2}\left[\frac{7}{8}\left(\Delta h\right)^2 - \frac{h_U^3+h_L^3}{h}\right], \tag{B9}$$

where $c_0 = \sqrt{\frac{g' h_U h_L}{h}}$ is the long wave phase speed, $g' = 2g\frac{\Delta\rho}{\rho_{00}}$, $\Delta\rho = \rho(z=0)-\rho(z=h)$, $\rho_{00} = \frac{1}{2}\left[\rho(z=h)+\rho(z=0)\right]$; $h_{U,L}$ denote the thickness of the layers above and below the pycnocline, with $\Delta h = h_U - h_L$ and $h = h_U + h_L$. Changing the variables (x,t) to (ξ,τ) in a coordinate frame moving to the right with the long wave speed c_0, and scaling the variables using characteristic scales for length L, time T and amplitude a of the perturbation

$$L\xi = x - c_0 t;\ T\tau = t;\ \eta = aq, \tag{B10}$$

with $\frac{T}{L} = \frac{L^2}{c_0\beta}$, obtains

$$q_\tau + s_2\sigma_2^2 q q_\xi + s_3\sigma_3^2 q^2 q_\xi + q_{\xi\xi\xi} = 0 \tag{B11}$$

where $s_j\sigma_j^2$, $j = 2,3$ are the quadratic and cubic Ursell numbers,

$$\sigma_2^2 = 9aL^2\frac{|\Delta h|}{h_U^2 h_L^2},\quad \sigma_3^2 = a^2L^2\frac{18}{\left(h_U h_L\right)^3}\left|\frac{7}{8}\left(\Delta h\right)^2 - \frac{h_U^3+h_L^3}{h}\right| \tag{B12}$$

with signs $s_2 = \operatorname{sign}\Delta h$ and $s_3 = \operatorname{sign}\left[\frac{7}{8}h\left(\Delta h\right)^2 - \left(h_U^3+h_L^3\right)\right]$. The Ursell numbers are used in the discussion in section 4.

References

Aksenov AV, Mozhaev VV, Skorovarov VE, et al (1987) Internal wave structure in a three-layer fluid with a stratified middle layer. Fluid Dynamics 22(3):437–441. https://doi.org/10.1007/BF01051925

Baines P (1982) On internal tide generation models. Deep Sea Research Part A Oceanographic Research Papers 29(3):307–338. https://doi.org/10.1016/0198-0149(82)90098-X

Bell JTH (1975) Topographically generated internal waves in the open ocean. Journal of Geophysical Research (1896-1977) 80(3):320–327. https://doi.org/10.1029/JC080i003p00320

Celona S, Merrifield ST, de Paolo T, et al (2021) Automated Detection, Classification, and Tracking of Internal Wave Signatures Using X-Band Radar in the Inner Shelf. Journal of Atmospheric and Oceanic Technology 38(4):789 – 803. https://doi.org/10.1175/JTECH-D-20-0129.1

Chiu LYS, Reeder DB (2013) Acoustic mode coupling due to subaqueous sand dunes in the South China Sea. The Journal of the Acoustical Society of America 134(2):EL198–EL204. https://doi.org/10.1121/1.4812862

Chiu LYS, Chang AYY, Reeder DB (2015) Resonant interaction of acoustic waves with subaqueous bedforms: Sand dunes in the South China Sea. The Journal of the Acoustical Society of America 138(6):EL515–EL521. https://doi.org/10.1121/1.4937746

Colosi JA, Kumar N, Suanda SH, et al (2018) Statistics of Internal Tide Bores and Internal Solitary Waves Observed on the Inner Continental Shelf off Point Sal, California. Journal of Physical Oceanography 48(1):123 – 143. https://doi.org/10.1175/JPO-D-17-0045.1

Doak A, Barros R, Milewski P (2022) Large mode-2 internal solitary waves in three-layer flows. Journal of Fluid Mechanics 953:A42. https://doi.org/10.1017/jfm.2022.974

Duda TF, Farmer DM (1999) The 1998 WHOI/IOS/ONR internal solitary wave workshop: contributed papers. Woods Hole Oceanographic Institution

Dysthe KB, Trulsen J (1989) Internal waves from moving point sources. John Hopkins APL Technical Digest 10(4):307–317

Edwards CR, Seim HE (2008) Complex eof analysis as a method to separate barotropic and baroclinic velocity structure in shallow water. Journal of Atmospheric and Oceanic Technology 25(5):808 – 821. https://doi.org/10.1175/2007JTECHO562.1

Egbert GD, Erofeeva SY (2002) Efficient inverse modeling of barotropic ocean tides. Journal of Atmospheric and Oceanic Technology 19(2):183–204

Egbert GD, Bennett AF, Foreman MGG (1994) Topex/poseidon tides estimated using a global inverse model. Journal of Geophysical Research: Oceans 99(C12):24821–24852

Farmer DM, Smith JD (1980) Tidal interaction of stratified flow with a sill in knight inlet. Deep Sea Research Part A Oceanographic Research Papers 27(3-4):239–254

Feddersen F, Barth J, Calantoni J, et al (2016) Inner Shelf Dynamics Science and Experiment Plan. Technical Report APL-UW 1602

Gardner CS, Greene JM, Kruskal MD, et al (1967) Method for solving the korteweg-devries equation. Phys Rev Lett 19:1095–1097. https://doi.org/10.1103/PhysRevLett.19.1095

Gerkema T, Zimmerman J (2008) An introduction to internal waves. Lecture Notes, Royal NIOZ, Texel 207

Gough MK, Chu PC, MacMahan JH, et al (2023) Diurnal Variability of Ocean Temperature Off Pt. Sal, Central California. Journal of Geophysical Research: Oceans 128(6):e2022JC018817. https://doi.org/10.1029/2022JC018817

Gregg MC (1989) Scaling turbulent dissipation in the thermocline. Journal of Geophysical Research: Oceans 94(C7):9686–9698. https://doi.org/10.1029/JC094iC07p09686

Grimshaw RHJ, Khusnutdinova KR (2004) Internal waves in a three-layer bubbly waveguide. Deep Sea Research Part II: Topical Studies in Oceanography 51(25):2905–2917. https://doi.org/10.1016/j.dsr2.2004.09.003

Grimshaw RHJ, Pelinovsky E, Talipova T, et al (2010) Internal solitary waves: propagation, deformation and disintegration. Nonlinear Processes in Geophysics 17(6):633–649

Gunn KL, Dickinson A, White NJ, et al (2021) Vertical mixing and heat fluxes conditioned by a seismically imaged oceanic front. Front Mar Sci 8(697179). https://doi.org/10.3389/fmars.2021.697179

Haury L, Wiebe P, Orr M, et al (1983) Tidally generated high-frequency wave packets and their effect on plankton in massachusetts bay. Journal of Marine Research 41:65–112. https://doi.org/10.1357/002224083788223036

Helfrich KR, Melville WK (2006) Long nonlinear internal waves. Annu Rev Fluid Mech 38:395–425. https://doi.org/10.1146/annurev.fluid.38.050304.092129

Holbrook WS, Páramo P, Pearse S, et al (2003) Thermohaline fine structure in an oceanographic front from seismic reflection profiling. Science 301(5634):821–824. https://doi.org/10.1126/science.1085116

Holloway PE (2001) Internal tide transformation and oceanic internal solitary waves. In: Grimshaw R (ed) Environmental Stratified Flows, Topics in Environmental Fluid Mechanics, vol Environmental Stratified Flows. Kluwer Academic Publishers, chap 1, p 29–60

Holloway PE, Pelinovsky E, Talipova T (1999) A generalized Korteweg-de Vries model of internal tide transformation in the coastal zone. Journal of Geophysical Research: Oceans 104(C8):18333–18350. https://doi.org/10.1029/1999JC900144

Hosegood P, Bonnin J, van Haren H (2004) Solibore-induced sediment resuspension in the faeroe-shetland channel. Geophysical Research Letters 31(9). https://doi.org/10.1029/2004GL019544

Jefferson J, Simeonov J, Calantoni J, et al (2025) Sediment resuspension on the inner shelf under combined internal tides and waves and surface waves: Field observations and modeling. Journal of Physical Oceanography 55(7):941–957. https://doi.org/10.1175/JPO-D-24-0074.1

Kamchatnov AM, Kuo YH, Lin TC, et al (2012) Undular bore theory for the Gardner equation. Phys Rev E 86(3):36605. https://doi.org/10.1103/PhysRevE.86.036605

Kaye GT (2005) Remote sensing of high-frequency internal waves with a narrow-beam echosounder. The Journal of the Acoustical Society of America 65(S1):S88–S88. https://doi.org/10.1121/1.2017492

Keller JB, Munk WH (1970) Internal wave wakes of a body moving in a stratified fluid. The Physics of Fluids 13(6):1425–1431. https://doi.org/10.1063/1.1693096

Klymak JM, Moum JN (2003) Internal solitary waves of elevation advancing on a shoaling shelf. Geophysical Research Letters 30(20). https://doi.org/10.1029/2003GL017706

Krahmann G, Brandt P, Klaeschen D, et al (2008) Mid-depth internal wave energy off the iberian peninsula estimated from seismic reflection data. Journal of Geophysical Research: Oceans 113(C12). https://doi.org/https://doi.org/10.1029/2007JC004678

Krishfield R, Toole J, Proshutinsky A, et al (2008) Automated ice-tethered profilers for seawater observations under pack ice in all seasons. Journal of Atmospheric and Oceanic Technology 25(11):2091 – 2105. https://doi.org/10.1175/2008JTECHO587.1

Kumar N, Suanda SH, Colosi JA, et al (2019) Coastal Semidiurnal Internal Tidal Incoherence in the Santa Maria Basin, California: Observations and Model Simulations. Journal of Geophysical Research: Oceans 124(7):5158–5179. https://doi.org/10.1029/2018JC014891

Kumar N, Lerczak JA, Xu T, et al (2021) The Inner-shelf Dynamics Experiment. Bulletin of the American Meteorological Society 102(5):E1033–E1063

694 Kurkina OE, Kurkin AA, Rouvinskaya EA, et al (2015) Propagation regimes of interfacial
695 solitary waves in a three-layer fluid. Nonlinear Processes in Geophysics 22(2):117–132
696 La Forgia G, Adduce C, Falcini F, et al (2019) Migrating bedforms generated by soli-
697 tary waves. Geophysical Research Letters 46(9):4738–4746. https://doi.org/10.1029/
698 2019GL082511
699 Large WG, Pond S (1981) Open ocean momentum flux measurements in moderate to
700 strong winds. Journal of Physical Oceanography 11(3):324–336. https://doi.org/10.1175/
701 1520-0485(1981)011<0324:OOMFMI>2.0.CO;2
702 Li Q, Farmer DM, Duda TF, et al (2009) Acoustical measurement of nonlinear internal
703 waves using the inverted echo sounder. Journal of Atmospheric and Oceanic Technology
704 26(10):2228 – 2242. https://doi.org/10.1175/2009JTECHO652.1
705 Ma X, Yan J, Hou Y, et al (2016) Footprints of obliquely incident internal solitary waves and
706 internal tides near the shelf break in the northern South China Sea. Journal of Geophysical
707 Research: Oceans 121(12):8706–8719. https://doi.org/10.1002/2016JC012009
708 McSweeney JM, Lerczak JA, Barth JA, et al (2019) Observations of shoaling nonlinear inter-
709 nal bores across the Central California inner shelf. Journal of Physical Oceanography
710 49(10):111–132. https://doi.org/10.1175/JPO-D-19-0125.1
711 Millero FJ, Poisson A (1981) International one-atmosphere equation of state of seawater.
712 Deep Sea Research Part A Oceanographic Research Papers 28(6):625–629. https://doi.org/
713 10.1016/0198-0149(81)90122-9
714 Miropol'sky YZ (2001) Dynamics of internal gravity waves in the ocean, vol 24. Springer
715 Science & Business Media
716 Nycander J (2005) Generation of internal waves in the deep ocean by tides. Jour-
717 nal of Geophysical Research: Oceans 110(C10). https://doi.org/https://doi.org/10.1029/
718 2004JC002487
719 Pelinovsky EN, Talipova TG, Stepanyants YA (1994) Modeling of nonlinear internal wave
720 propagation in the horizontally inhomogeneous ocean. Izvestiâ Akademii nauk SSSR
721 Fizika atmosfery i okeana 30(1):79–85
722 Pica A, Diet JP, Tarantola A (1990) Nonlinear inversion of seismic reflection data in a laterally
723 invariant medium. GEOPHYSICS 55(3):284–292. https://doi.org/10.1190/1.1442836
724 Proni JR, Apel JR (1975) On the use of high-frequency acoustics for the study of internal
725 waves and microstructure. Journal of Geophysical Research (1896-1977) 80(9):1147–
726 1151. https://doi.org/https://doi.org/10.1029/JC080i009p01147
727 Quaresma LS, Vitorino J, Oliveira A, et al (2007) Evidence of sediment resuspension by
728 nonlinear internal waves on the western portuguese mid-shelf. Marine geology 246(2-
729 4):123–143
730 Reeder DB, Ma BB, Yang YJ (2011) Very large subaqueous sand dunes on the upper con-
731 tinental slope in the South China Sea generated by episodic, shoaling deep-water internal
732 solitary waves. Marine Geology 279(1):12–18. https://doi.org/10.1016/j.margeo.2010.10.
733 009
734 Ruddick B, Song H, Dong C, et al (2009) Water column seismic images as maps of tem-
735 perature gradient. Oceanography 22(1):192 – 205. https://doi.org/10.5670/oceanog.2009.
736 19
737 Shakespeare CJ (2020) Interdependence of internal tide and lee wave generation at abyssal
738 hills: Global calculations. Journal of Physical Oceanography 50(3):655 – 677. https://doi.

org/10.1175/JPO-D-19-0179.1
Shakespeare CJ, Arbic BK, Hogg AM (2020) The drag on the barotropic tide due to the generation of baroclinic motion. Journal of Physical Oceanography 50(12):3467 – 3481. https://doi.org/10.1175/JPO-D-19-0167.1
Sheen KL, White NJ, Hobbs RW (2009) Estimating mixing rates from seismic images of oceanic structure. Geophysical Research Letters 36(24). https://doi.org/10.1029/2009GL040106
Slyunyaev AV, Pelinovski EN (1999) Dynamics of large-amplitude solitons. Journal of Experimental and Theoretical Physics 89(1):173–181. https://doi.org/10.1134/1.558966
Smith SGL, Young WR (2002) Conversion of the barotropic tide. Journal of Physical Oceanography 32(5):1554 – 1566. https://doi.org/10.1175/1520-0485(2002)032<1554:COTBT>2.0.CO;2
Toole JM, Timmermans ML, Perovich DK, et al (2010) Influences of the ocean surface mixed layer and thermohaline stratification on arctic sea ice in the central canada basin. Journal of Geophysical Research: Oceans 115(C10). https://doi.org/https://doi.org/10.1029/2009JC005660
Tseluiko D, Alharthi NS, Barros R, et al (2023) Internal ring waves in a three-layer fluid on a current with a constant vertical shear. Nonlinearity 36(6):3431. https://doi.org/10.1088/1361-6544/accfe0
Waterhouse AF, McSweeney JM, Barth JA, et al (2020) Observations and Model Simulations from the Inner-Shelf Dynamics Experiment (ISDE), 2020, https://doi.org/10.6075/J0WD3Z3Q, uC San Diego Library Digital Collections.
Zulberti A, Jones NL, Ivey GN (2020) Observations of enhanced sediment transport by nonlinear internal waves. Geophysical Research Letters 47(19):e2020GL088499